NRC Research Press

ARTICLE

Synthesis, optical properties, and amplified spontaneous emission of hybrid Ag–SiO_2–CdTe nanocomposite

A.M. Saad, M.B. Mohamed, and I.M. Azzouz

Abstract: In this work, a hybrid nanocomposite of metal–dielectric–semiconductor, Ag–SiO_2–CdTe, nanoparticles has been synthesized. Silica shell was used as a spacer to isolate and control the distance between Ag plasmonic and luminescent CdTe QDs. It was found that insertion of silica shell enhances the plasmonic field more than 31%. Accordingly, Ag-SiO_2 plasmonic enhances the luminescence and quantum yield of CdTe quantum dots by 200% and 55%, respectively. The threshold power of amplified spontaneous emission of CdTe was found to depend on both temperature and excitation wavelength location with respect to plasmon and exciton absorption. This nanocomposite could be potentially used in light-emitting diodes, biological sensing, and thermal therapy.

Key words: plasmon, quantum yield, amplified spontaneous emission, nanocomposite of metal–dielectric–semiconductor, decay lifetime.

Résumé : Nous synthétisons ici un nanocomposite hybride, à savoir une nanoparticule métal–diélectrique–semiconducteur de Ag–SiO_2–CdTe. La couche de silice sert d'intercalaire pour isoler et contrôler la distance entre l'Ag plasmonique et le point quantique luminescent CdTe. Nous trouvons que la couche de silice augmente le champ plasmonique de plus de 31 %. Ainsi, l'Ag–SiO_2 plasmonique augmente la luminescence et le rendement quantique de 200 % et de 55 % respectivement. Nous trouvons que le seuil de puissance de l'émission spontanée amplifiée du CdTe dépend à la fois de la température et de la localisation de la longueur d'onde d'excitation par rapport à l'absorption du plasmon et de l'excitation. Cette nanoparticule composite a le potentiel pour être utilisée dans les diodes électroluminescentes, la détection en biologie et en thérapie thermique. [Traduit par la Rédaction]

Mots-clés : plasmon, rendement quantique, émission spontanée amplifiée, nanocomposite de métal-diélectrique-semiconducteur, temps de vie sous désintégration.

1. Introduction

Interaction of metal–semiconductor nanoparticles (NPs) is an important field in nanophotonic science. Semiconductor NPs are characterized by bandgap tunability according to their size and shape [1]. This allows for different technological applications, such as light-emitting diodes (LED) [2, 3], nanolaser [4], photo-nano sensors [5], and solar cells [6].

Metallic nano-systems are characterized by plasmonic fields, which may be classified as volume plasmon, surface plasmon (SP) polaritons, and localized surface plasmons (LSP). The intensity of plasmonic modes depends on electromagnetic (EM) pump frequency. Plasmonic propagation does not emit light, but creates a strong local field to excite the nearby active molecules (such as dyes or semiconductor NPs). Semiconductor NPs in the vicinity of metallic NPs exhibit changes in their optical and lasing properties depending on their size, shape, relative concentration ratio, and intra-distance [7], in addition to the EM pump frequency [8]. A temporally coherent high-intensity field can be generated by plasmonics on metallic-nanosystem surface known as SPASER [8, 9] (surface plasmon amplification by stimulated emission of radiation). This differs from traditional laser, in which photon amplification is obtained by amplified spontaneous emission (ASE), the important parameter in the lasing process.

In SPs, a near-field phenomenon of surface electron oscillations is created by interactions of incident EM wave with free electrons in nano-metals. Resonant excitation of metallic NPs forms high LSP of strong EM field and good spatial confinement in the sub-wavelength scale. Thus their propagation avoids the limitation imposed by diffraction [9]. Nano-size metal–dielectric interface assists some special EM modes, such as LSP or SP polariton, to propagate along their interface, where an incident EM wave induces oscillation of metallic electrons at the dielectric boundary. The energy transfer from the gain medium to SPs excites SP resonance mostly with the same mode yielding more plasmonic modes available for lasing radiation [9].

CdTe quantum dots (QDs) are an important II–VI semiconductor [10] of high luminescence quantum yield. They has wide applications in many fields. The present work studied the optical properties of CdTe QDs for the lasing process in the presence and absence of metal–dielectric plasmons. Firstly, we explored synthesis methods and the optical properties of CdTe QDs, Ag NPs, Ag–SiO_2 core–shell NPs, and hybrid Ag–SiO_2–CdTe nanocomposite. Secondly, we studied the effect of metal–dielectric Ag–SiO_2 core–shell on lasing properties (luminescence power dependence and relaxation dynamics) of CdTe QDs.

2. Experimental

2.1. Materials and reagents

The chemicals used for synthesis were: silver nitrate ($AgNO_3$, 99.8%, SIGMA-ALDRICH), sodium citrate ($Na_3C_6H_5O_7$•$7H_2O$, MOISTURE),

Received 27 May 2016. Accepted 21 March 2017.

A.M. Saad, M.B. Mohamed, and I.M. Azzouz. National Institute of Laser Enhanced Science, Cairo University, Cairo University Street, Giza, Egypt, 12613.
Corresponding author: A.M. Saad (email: ahmedsaad@niles.edu.eg).

ethanol (C_2H_5OH, ADWIC), ammonia (NH_3, 33%, ADWIC), tetraethylorthosilicate (TEOS, 98%, FLUCKA), sodium borohydride ($NaBH_4$, 97%, ALPHA), tellurium powder (Te, 99.8%, ALDRICH), cadmium chloride ($CdCl_2$•$2.5H_2O$, 99%, WINLAB), 3-mercaptopropionic acid (MPA, 98%, MERCK), 3-aminopropyltriethoxysilane (APS, 99%, SIGMA-ALDRICH), and sodium hydroxide (NaOH, 98%, RIEDEL-DE HAEN). All the chemicals used were of the highest purity available. For aqueous solution, double distilled water was used.

2.2. Experimental procedures

2.2.1. Synthesis of Ag NPs

A colloidal Ag NP solution was synthesized by reducing $AgNO_3$ with sodium citrate in an aqueous solution [11]. In detail, 1.7 mmol/L of $AgNO_3$ was dissolved in 200 mL of water with stirring and the solution was heated to boiling point, then 10 mL of 1% trisodium citrate was added dropwise with stirring until it became pale yellow, at which point it was left to cool with stirring for 1 h.

2.2.2. Preparation of Ag–SiO_2 core shell NPs

Ag–SiO_2 core shell was prepared following the Stöber method [12] where 1.67 mmol/L of colloidal Ag NP solution was stirred with 0.718 mol/L of ethanol and 24 mmol/L of ammonia. Ethanol and ammonia were added to activate the surface of the Ag NPs. TEOS was then added and the mixture was stirred for several days. The formed thickness of the silica shell depends on the relative concentrations of TEOS, ammonia, and Ag NPs.

The transparent dielectric silica shell around the NPs has the potential to modify and stabilize the plasmonic properties [13] with many possibilities for surface modification. Coating with silica in a seeded growth process decreased the poly-dispersity of NPs and reduces Van der Waals attraction, so the colloid stability and ability to form colloidal crystals enhances. It also increases the mechanical stability, makes possible transfer into organic solvents, provides a capping layer on the semiconductor nanocrystals, and protects metal particles against oxidation.

2.2.3. Preparation of CdTe QDs

Aqueous colloidal solution of CdTe QDs was prepared in the reaction between Cd^{+2} and NaHTe solution in the presence of MPA as a stabilizer [14]. NaHTe was first prepared as a precursor of Te by heating a mixture of Te powder (0.3 mol/L) and $NaBH_4$ (0.6 mol/L) with deionised water (10 mL) at 60 °C in a water path for 30 min. Hydrogen was released through a small outlet of the tube where white precipitation of sodium tetra-borate was formed. The color of NaHTe solution was violet and NaHTe was separated using a filter paper. The Cd^{+2} precursor was prepared by mixing $CdCl_2$•H_2O solution with 3-mercaptopropionic acid (MPA) at adjusted pH of 7.5 using 1 mol/L of NaOH. Then, Cd^{+2}/MPA and NaHTe precursors were mixed at molar ratio 1:2.4:1. Equal volumes of this mixture were exposed to microwaves at different powers. Finally, CdTe QDs were mixed with isopropanol and centrifuge at 5000 rpm to precipitate.

2.2.4. Preparation of hybird Ag–SiO_2–CdTe nanocomposite

To connect CdTe NPs with Ag–SiO_2 NPs, the surface of the silica shell was activated. This was done by modifying the surface of the silica shell with a layer of APS to decrease their distance to CdTe QDs (the effective parameter in energy transfer). This layer was formed by adding 25 μL of APS (1 mmol/L) to Ag–SiO_2 NPs (1 mmol/L) with stirring for 15 min. CdTe NPs was then added to Ag–SiO_2–APS at molar ratio 50:1 and the mixture was stirred at 500 rpm for 12 h. The silanol group (Si–OH) of APS was connected to the silica layer so the surface of the Ag–SiO_2 core–shell becomes active with the amino group. The amino group of the modified surface attracted to COOH of CdTe QDs, so the CdTe QDs were self-assembled on the core–shell surface forming hybrid Ag–SiO_2–CdTe nanocomposite.

Fig. 1. Setup of laser-induced florescence (LIF). [Colour online.]

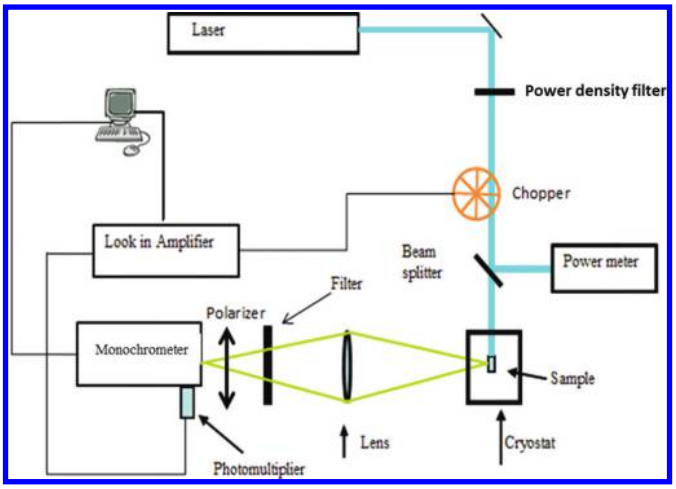

2.3. Physical characterization

2.3.1. X-ray diffraction (XRD) measurements

Crystalline structure of the samples was investigated using XRD powder diffractometer (XPERT-PRO-PANalytical, the Netherlands) operating with Cu anode. The samples were precipitated using 2-isopropanol and washed with water then translated on a glass substrate for investigation.

2.3.2. High-resolution transmission electron microscopy (TEM) and energy dispersive X-ray spectroscopy (EDX)

High-resolution TEM (Tecnai G20, FEI, Netherland) and EDX were used for the purpose of imaging, crystal structure revelation, and elemental analysis. Two different modes of imaging were employed: the bright field at electron accelerating voltage 200 kV, using lanthanum hexaboride (LaB6) electron source gun, and the diffraction pattern imaging. Eagle CCD camera with (4k × 4k) image resolution was used to acquire and collect transmitted electron images. TEM Imaging & Analysis (TIA) software was used for spectrum acquisition and analysis of EDX peaks. A drop of a very dilute sample solution was deposited on an amorphous carbon–copper grid and left to evaporate at room temperature.

2.3.3. Laser-induced fluorescence (LIF) with temperature control

The LIF technique was applied to measure the fluorescence of the prepared NP samples. An argon laser of 488 nm was used to excite the samples at low temperatures (50 K) and fluorescence was detected using a spectrometer. A schematic diagram of LIF experimental setup is shown in Fig. 1.

2.3.4. Nanosecond relaxation dynamics

Lifetime measurement of excited levels in a fluorescent medium is important for lasing properties. In the present measurements, the excitation source was a pulsed N_2 laser (337 nm wavelength) of 800 ps pulse duration and maximum pulse energy of 2 mJ. The laser was focused as a line on the samples by a cylindrical lens. Emission was collected by a lens on a fast photo-tube connected to an oscilloscope (300 MHz) of 1 ns resolution time.

Curve fitting of the measured time evolution data were carried out using OrginLab v. 8, applying either first- or second-order exponential decay with offset fitting equations

$$y = A_1 \exp\left(\frac{-t}{\tau_1}\right) + y_0 \quad (1)$$

$$y = A_1 \exp\left(\frac{-t}{\tau_1}\right) + A_2 \exp\left(\frac{-t}{\tau_2}\right) + y_0 \quad (2)$$

Fig. 2. TEM at scale bars 20 nm of (*a*) Ag NPs, (*b*) Ag–SiO_2 NPs core-shell silica shell thickness is 8 nm. (*c*) CdTe QDs with average nano-size 3 nm. (*d*) hybrid Ag–SiO_2–CdTe nanocomposite. [Colour online.]

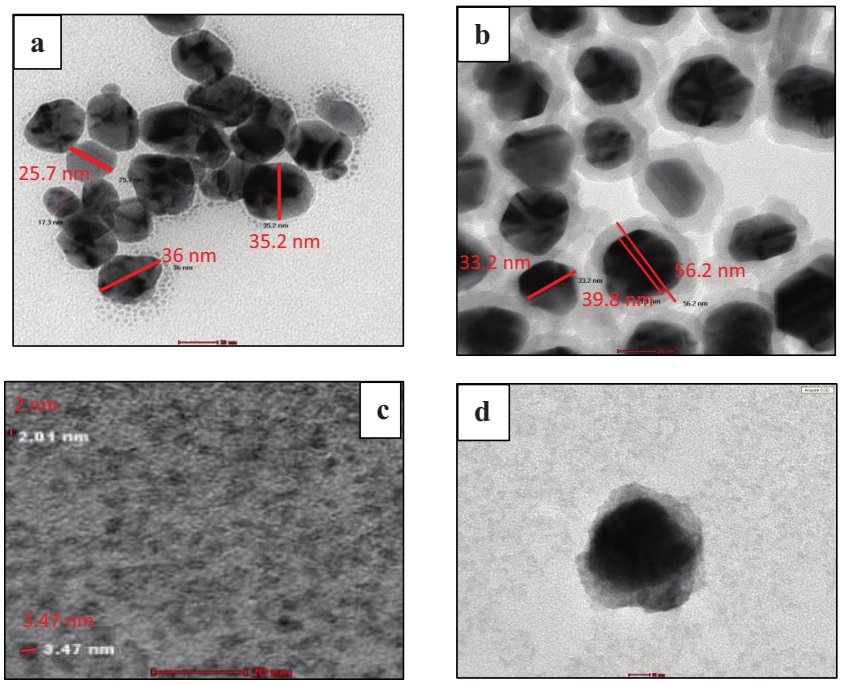

Fig. 3. XRD of Ag NPs, Ag–SiO_2 core–shell NPs, CdTe QDs, and hybrid Ag–SiO_2–CdTe nanocomposite.

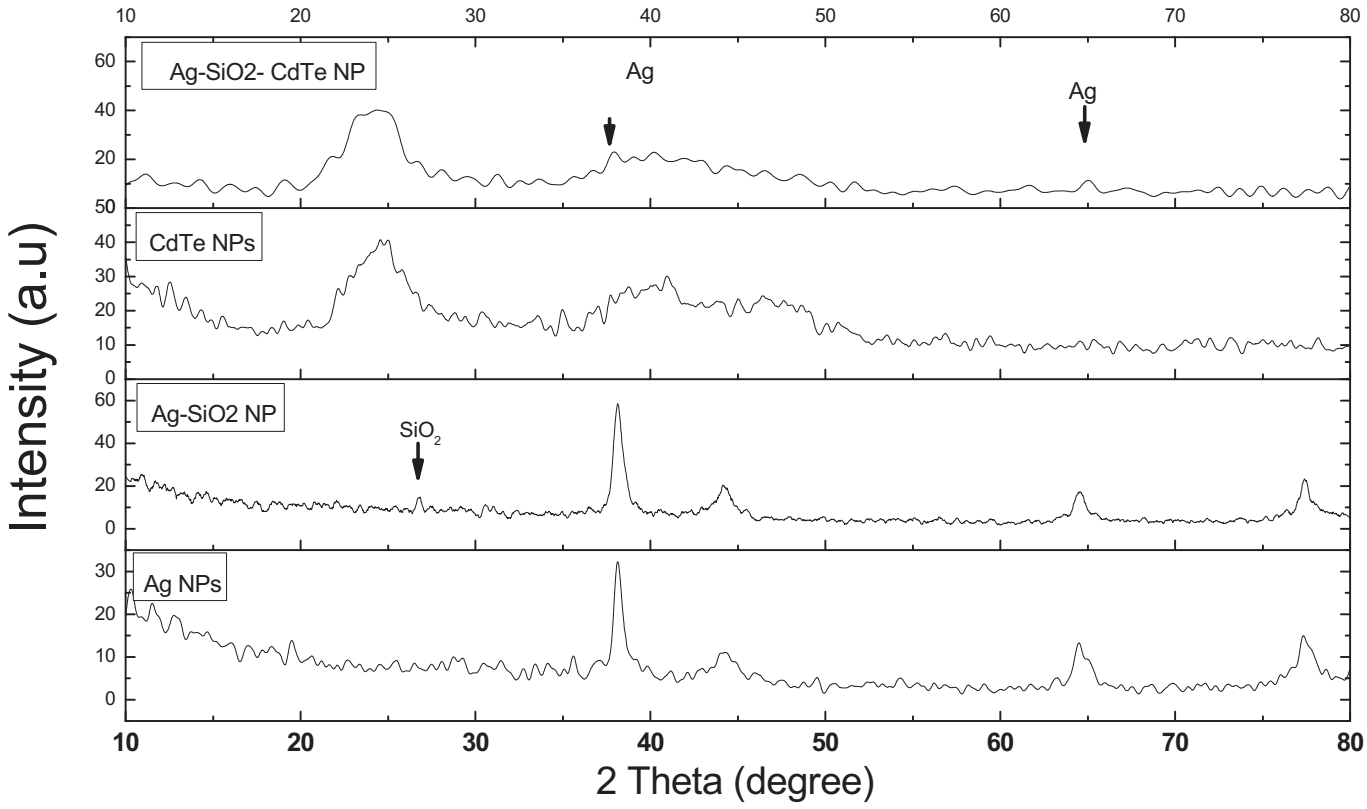

Fig. 4. (*a*) Absorbance spectra of Ag NPs (black line) and Ag–SiO_2 core–shell NPs (red line) at same molarity of Ag NPs. (*b*) Absorbance and fluorescence spectra of; fluorescein dye (curves 1 and 2), CdTe QDs (curves 3 and 4), and hybrid Ag–SiO_2–CdTe nanocomposite (curves 5 and 6). Excitation wavelength is 405 nm. [Colour online.]

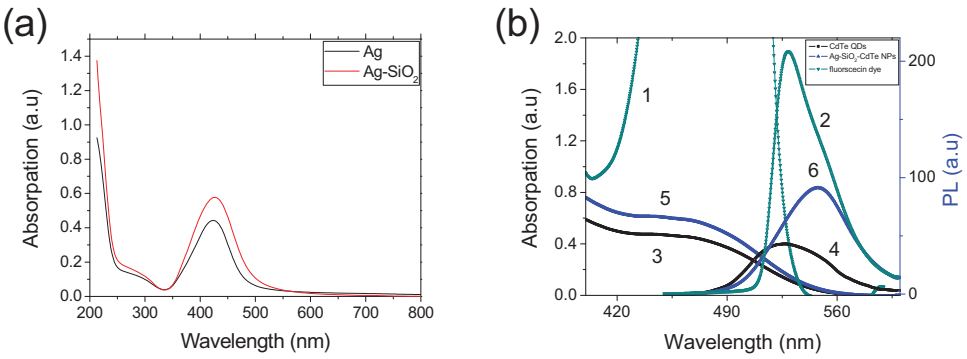

3. Results and discussion

The formation and structure of the prepared NPs were first investigated using TEM and XRD techniques. Figures 2*a*–2*d* present TEM images of Ag NPs, Ag–SiO_2 NPs core–shell, CdTe QDs, and hybrid Ag–SiO_2–CdTe nanocomposite, respectively. Figure 2*a* shows Ag NPs with average diameter of nearly 30 nm. In Fig. 2*b*, the coated thin layer of silica around Ag NPs appears to be of an average thickness of 8 nm. Figure 2*c* shows the prepared CdTe QDs with average diameter of 3 nm. Figure 2*d* shows a TEM image of hybrid Ag–SiO_2–CdTe nanocomposite where CdTe QDs are self-assembled around the surface of Ag–SiO_2 core–shell.

Figure 3 shows XRD at various formation stages of hybrid Ag–SiO_2–CdTe nanocomposite. XRD revealed cubic crystal structure of Ag NPs, which was characterized by four distinct features at $2\theta = 38.1°$, 44.2°, 64.4°, and 77.4°, which were attributed to reflection at planes (111), (200), (220), and (311), respectively [15]. Silica shell revealed α-quartz hexagonal structure characterized by distinct feature at $2\theta = 26.7°$ due to (011) reflection [16]. CdTe QDs displays a zinc blende cubic structure characterized by a feature at $2\theta = 25°$, due to (111) reflection, two broad features at $2\theta = 40°$ and 47° due to (220) and (311) reflections, respectively, and a shoulder at $2\theta = 30°$ due to plane (200) [17]. XRD of Ag–SiO_2–CdTe hybrid nanocomposite displays combined features of all Ag NPs, silica shell, and CdTe QDs.

Figure 4*a* compares the absorption spectrum of Ag–SiO_2 core–shell to that of Ag NPs, at 1 mmol/L of Ag NPs. Ag–SiO_2 core–shell shows higher absorption intensity more than 31% with broadening of 11 nm in full width at half maximum (FWHM). These enhancements were attributed to the presence of dielectric silica shell layer, which has the potential to modify the plasmonic properties [13].

Figure 4*b* compares the absorption and photoluminescence (PL) of hybrid Ag–SiO_2–CdTe nanocomposite to those of CdTe QDs at constant concentration of the active fluorescent (3 mmol/L of CdTe QDs). Comparisons was carried out in reference to the standard diluted fluorescein dye (0.1 mol/L NaOH(aq)), which displays high quantum yield (0.925 ± 0.015) [18] in the same spectral region (curves 1 and 2 in Fig. 4*b*). The figure showed ~31% enhancement in the absorption of hybrid Ag–SiO_2–CdTe nanocomposite compared to that of CdTe QDs. This enhancement in the absorption rate of CdTe NPs was attributed to propagation of LSP on the surface of Ag–SiO_2 core–shell [19, 20]. Also, an enhancement by ~200% was reported for the luminescence of hybrid Ag–SiO_2–CdTe nanocomposite compared to that of CdTe QDs. This luminescence enhancement was attributed to the presence of a silica shell, which allows for energy transfer from the Ag NP core to CdTe QDs and prevents electron transfer from CdTe QDs to Ag NPs core [19, 20]. Also, fluorescence spectra displayed Stokes shift of the order of 21 nm associated with 3.6 nm narrowing in FWHM. This was also attributed to coupling between QDs and local SPs of metal (strong dipole–dipole interaction between plasmon and exciton coupling).

Fig. 5. Schematic energy diagram for physical process: excitation (blue arrow); radiative decay (red arrow); non-radiative decay and plasmon transfer (axial arrow) between Ag NPs and CdTe QDs; excitation wavelength (λ_{ex}) excited electrons of Ag NPs to oscillate generating electric fields (plasmon modes) which propagate and transport in silica layer to CdTe QDs causes enhancement in radiative decay rate (γ_r) of CdTe QDs and absorption rate (γ_{abs}) and decreased the non-radiative decay rate (γ_{nr}). Silica shell prevents electron transfer from CdTe QDs to Ag NPs. [Colour online.]

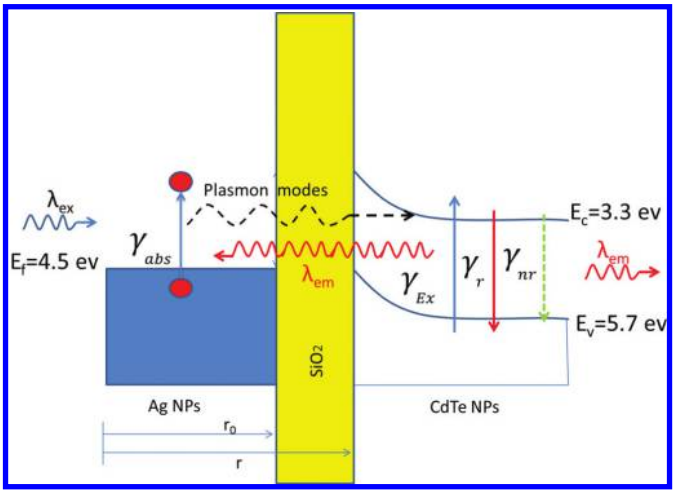

The quantum yield was calculated according to the following equation:

$$Q_{NC} = \frac{I_{NC}}{I_{Dye}} \frac{OD_{Dye}}{OD_{NC}} Q_{Dye} \quad (3)$$

where *I* is the integrated emission spectrum and OD is the optical density for the dye and nanocrystals. The quantum yields of CdTe QDs and hybrid Ag–SiO_2–CdTe nanocomposite were estimated to be 47% and 73%, respectively. The enhancement in quantum yield value can be interpreted in reference to Fig. 5 as in the next paragraph.

Fig. 6. Low temperature (50 K) PL for (*a*) CdTe QDs, and (*b*) hybrid Ag–SiO_2–CdTe nanocomposite, embedded in PVA polymeric films. Inset: power dependence curve of PL intensity and FWHM. Excitation wavelength was 488 nm. [Colour online.]

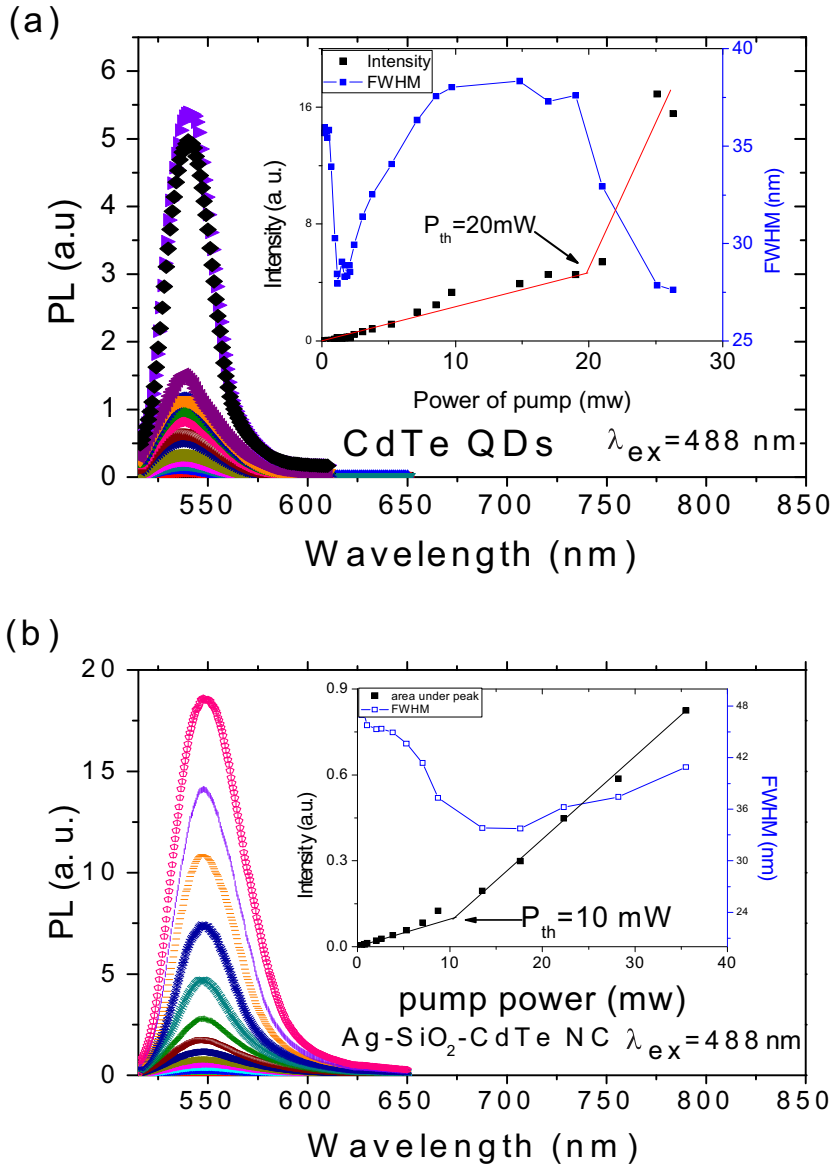

Figure 5 presents a schematic energy diagram for the physical processes: absorption, radiative, and non-radiative decays and plasmon transfer between luminescent CdTe and Ag NPs in the presence of silica shell barrier. The diagram shows that an incident radiation at wavelength λ_{ex} excites CdTe QDs at excitation decay rate γ_{ex}, and is absorbed by Ag NPs at absorption rate γ_{abs}. The latter generates plasmon modes propagated through the silica shell barrier towards CdTe QDs. In the case of in-resonance, plasmon field enhances γ_{ex}, which in turn enhances the radiative decay rate γ_r (fluorescence) [19, 20]. It is worth mentioning that excitation decay rate (γ_{Ex}) depends on excitation wavelength λ_{ex}, nano-metal size and shape, and plasmon strength, which is a function of distance between Ag NPs and CdTe QDs [20]. The figure also shows the emitted photons from CdTe QDs, at wavelength λ_{em}, which transfer to Ag NPs through silica barrier leading to plasmon enhancement. In addition, CdTe quantum yield changed according to the change in radiative decay rate (γ_r), intrinsic non-radiative decay (γ_{nr}), and Ag NPs absorption rate (γ_{abs}). γ_r increased with plasmon field strength, but γ_{abs} depends on λ_{em} therefore re-absorption is maximized if λ_{em} is in-resonance with the peak band of Ag NPs (422 nm) [20]. This induced a reduction in γ_{nr} and increases the γ_r, which in-turn enhances the net quantum yield according to the formula

$$Q = \frac{\gamma_r}{\gamma_r + \gamma_{nr}} \tag{4}$$

Stimulated emission measurements were carried out for both CdTe QDs and hybrid Ag–SiO_2–CdTe nanocomposite samples at constant concentration of CdTe QDs. The samples were embedded in PVA polymeric films to carry out measurements at low temperature (50 K) without changing the transparency of the samples. Measurements were performed at 50 K to reduce thermal effects, such as auger process, surface trapping, and phonon contributions. The samples were excited by a 488 nm Ar laser at different powers (0.1–50 mW). This wavelength is located within the absorp-

tion spectral range of both CdTe QDs and Ag–SiO_2 NPs (in-resonance). The measured PL-power-dependent data for both CdTe QDs and hybrid Ag–SiO_2–CdTe nanocomposite are presented in Figs. 6*a* and 6*b*, respectively. The figures show a fast increase in PL intensity upon pumping by powers >20 mW for CdTe QDs and >10 mW for hybrid Ag–SiO_2–CdTe nanocomposite. The increase in intensity accompanied with a narrowing of FWHM from 38 to 27 nm for CdTe QDs and from 47 to 33 nm for hybrid Ag–SiO_2–CdTe nanocomposite. The fast increase in PL indicates the onset of ASE. The reported reduction in ASE threshold power of hybrid Ag–SiO_2–CdTe nanocomposite compared to that of CdTe QDs was attributed to the presence of Ag–SiO_2 core–shell SP.

Figures 7*a*–7*c* show normalized PL of hybrid Ag–SiO_2–CdTe nanocomposite embedded in PVA polymeric films. PL was detected at 50 K upon excitation by Ar laser at 488 nm. Figure 7*a* compares PL due to excitation at a low pump power, 1 mW (red curve), with a little higher excitation power, ~11 mW (black curve), very close to the ASE threshold power. PL at 1 mW (red curve) shows a single symmetric peak, from exciton state only. PL at ~11 mW (black curve) shows a red-shifted non-symmetrical peak with broadening in FWHM, which attributed to emission from both exciton (X) and biexciton (XX) associated to the $1S_e$–$1S_h$ transition.

At low pump powers, the formation probability of X (e-hole pair) is higher than that of multi-exciton (more than one exciton per dot). As pump power increases, formation of multi-exciton becomes more probable [21].

Figure 7*b* compares PL due to excitation at ~11 mW (ASE threshold power) to that at a higher power ~25 mW (red and black curves). PL at the higher excitation is red-shifted by ~4 nm (≈17 meV) with a narrowing in FWHM. PL of XX is red-shifted about PL of X by 4 nm (17 meV) in relation with binding energy of XX [22, 23]. The accompanied reduction in FWHM (~11 nm) is attributed to overlapping between ASE from XX state with the residual spontaneous emission of X state [22]. This overlapping was examined in Fig. 7*c* by fitting the PL data using pseudo-Voigt function. The fitting shows two symmetric peaks due to exciton (X) (red curve) and biexciton (XX) (green curve) where intensity due to XX is four times higher than that of residual spontaneous emission from X state.

The ASE measurements at 50 K were repeated for both CdTe QDs and Ag–SiO_2–CdTe nanocomposite using a diode laser of 405 nm. The results are presented in Figs. 8*a* and 8*b*, respectively. This excitation wavelength located in-resonance with the absorption peak of Ag–SiO_2 core–shell but off-resonance with absorption $1S_h$–$1S_e$ state of CdTe QDs. The measurements yielded ASE threshold powers of 26 mW for CdTe QDs (inset of Fig. 8*a*) and 36 mW for hybrid Ag–SiO_2–CdTe nanocomposite (inset of Fig. 8*b*). These threshold powers are higher than those obtained on excitation by 488 nm (20 and 10 mW, respectively). The increment in threshold powers was nearly 30% for CdTe QDs and 260% for hybrid Ag–SiO_2–CdTe nanocomposite. These increments were attributed to the following: in the case of CdTe QDs, excitation was to higher states (2S, 2P, ...), which decayed non-radiatively to 1S state, while in the case of hybrid nanocomposite, excitation wavelength mismatches the resonance of exciton–plasmon interaction, so most absorbed energy by Ag–SiO_2 is dissipated non-radiatively.

ASE of QDs is related to population inversion, which was achieved when the density of electron–hole pairs is more than 1.4 [24]. This means that above threshold power, biexciton state formed in the majority of the particles. The lifetimes of X and XX in CdTe QDs and hybrid Ag–SiO_2–CdTe nanocomposite are studied in Fig. 9. The fluorescence decay lifetimes were measured using pulsed N_2 laser (337 nm, pulse duration 800 ps). As the lifetime depends on formation of exciton and biexciton, therefore excitation was obtained at two different pump energies: 0.1 and 0.7 mJ. At lower pump energy, the probability of forming a single

Fig. 7. Normalized PL of hybrid Ag–SiO_2–CdTe nanocomposite embedded in PVA polymeric film and detected at 50 K on excitation by 488 nm at powers: (*a*) 1 mW and at ASE threshold power (~11 mW), (*b*) ~11 mW and above threshold power of ASE (~25 mW), (*c*) fitting of PL for (~25 mW) using pseudo-Voigt function. [Colour online.]

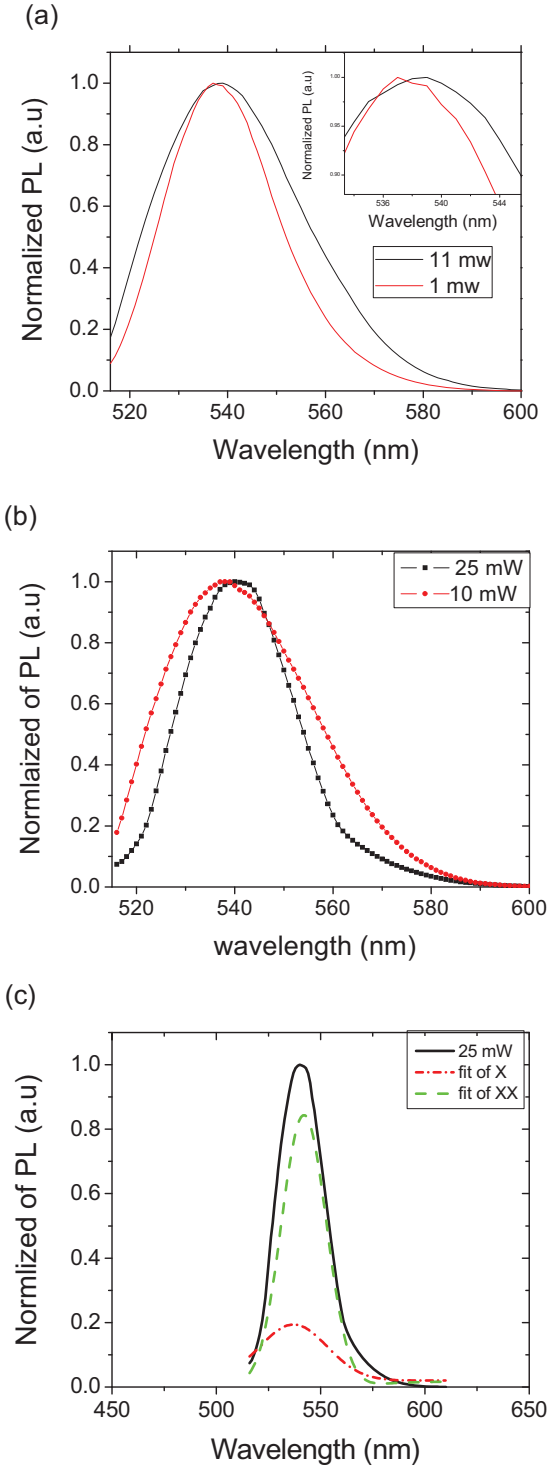

X is higher than that of XX; therefore, lifetime is related to exciton formation only, so (1) was applied.

At higher pump energy, the probability of biexciton formation increased, therefore fluorescence lifetime is due to formation of

Fig. 8. Low temperature (50 K) PL for (*a*) CdTe QDs, and (*b*) hybrid Ag–SiO_2–CdTe nanocomposite, embedded in PVA polymeric films. Inset: power dependence curve of PL intensity and FWHM. Excitation wavelength was 405 nm. [Colour online.]

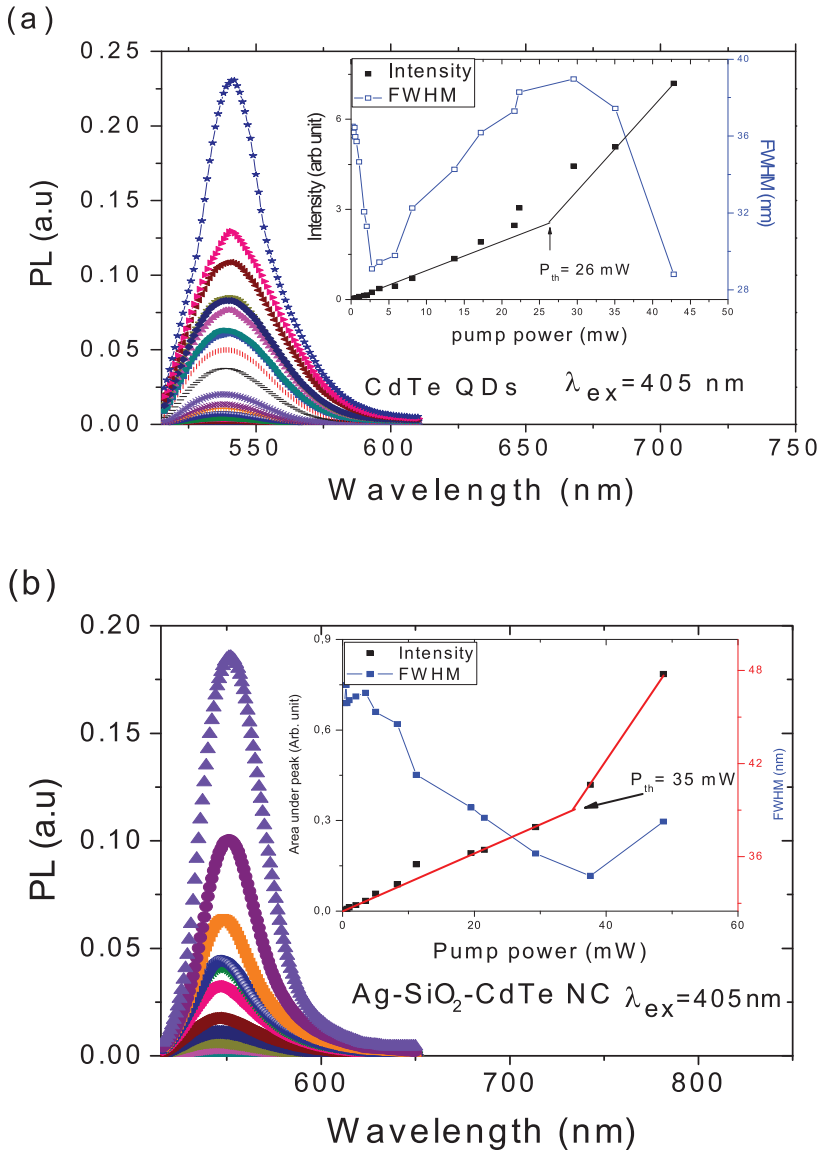

Fig. 9. Relaxation time at pump energies 0.1 and 0.7 mJ for (*a*) CdTe QDs, and (*b*) hybrid Ag–SiO_2–CdTe nanocomposite. [Colour online.]

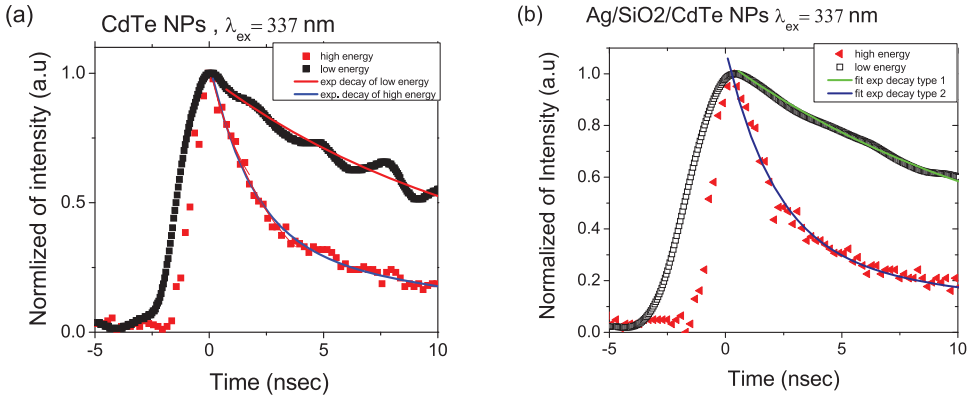

both exciton and biexciton. Figure 9 presents the experimentally measured lifetimes at low and high pump energies (symbols) together with their fitted curves using first- and second-order exponential decay equations, respectively. For both CdTe QDs and hybrid Ag–SiO_2–CdTe nanocomposite, lifetimes were calculated to be typically 13 ns for exciton and 2 ns for biexciton.

4. Conclusion

In this work, we synthesized hybrid Ag–SiO_2–CdTe nanocomposite to optimize the ASE of CdTe QDs. Synthesis was carried out via three stages. Firstly, CdTe QDs were prepared using the microwave-assisted organic aqueous method. Secondly, Ag NPs were synthesized by reducing $AgNO_3$ with sodium citrate in an aqueous solution, then coating them with a thin layer of dielectric silica to modify and stabilize the plasmonic properties. Silica shell was formed by hydrolysis and condensation of TEOS with ammonia. The surface of Ag–SiO_2 core–shell was treated with APS to decrease the distance to CdTe QDs and to enhance energy transfer. CdTe QDs were self-assembled on Ag–SiO_2 core–shell surface, yielding the hybrid Ag–SiO_2–CdTe nanocomposite.

Characterizations of structural and optical properties were obtained by XRD, TEM image, and absorption and emission spectra. The results confirmed the formation NPs at different stages of hybrid nanocomposite synthesis. The transparent silica layer around Ag NPs enhances the LSP and prevents electron transfer from CdTe QDs to Ag NPs. This led to enhanced luminescence and quantum yield of CdTe QDs. In addition, LSP decreased the ASE threshold power of the CdTe QDs gain medium by 50% upon excitation by a wavelength in-resonance with absorbance of plasmon–exciton coupling. Otherwise, on pumping by an off-resonance wavelength, LSP increases the ASE threshold power of CdTe QDs gain medium. In addition, on pumping by an above-threshold power, reduction was observed in FWHM of both CdTe QDs and hybrid Ag–SiO_2–CdTe nanocomposite (~10 and ~14 nm, respectively). Lifetime measurements of exciton and biexciton yielded 13 and 2 ns, respectively.

Acknowledgements

The authors are grateful to the team at the semiconductor lab in Laser Science and Interaction Department, National Institute of Laser Enhanced Sciences, Cairo University, for their help in carrying out temperature control laser induced fluorescence experiment.

References

1. D.J. Norris, A.L. Efros, M. Rosen, and and M.G. Bawendi. Phys. Rev. B, **53**, 16347 (1996). doi:10.1103/PhysRevB.53.16347.
2. Q. Qiao, C.-X. Shan, J. Zheng, B.-H. Li, Z.-Z. Zhang, and and D.-Z. Shen. J. Lumin. **134**, 754 (2013). doi:10.1016/j.jlumin.2012.06.052.
3. A.H. Mueller, M.A. Petruska, M. Achermann, D.J. Werder, E.A. Akhadov, D.D. Koleske, M.A. Hoffbauer, and and V.I. Klimov. Nano Lett. **5**, 1039 (2005). doi:10.1021/nl050384x. PMID:15943439.
4. M.A. Noginov, G. Zhu, A.M. Belgrave, et al. Nature, **460**, 1110 (2009). doi:10.1038/nature08318. PMID:19684572.
5. K. Shimanoe, M. Yuasa, T. Kida, and N. Yamazoe. *In* IEEE Nanotechnol. Mater. Devices Conf. 2011. pp. 38.
6. J. Tian and G. Cao. Nano Rev. **4**, 22578 (2013). doi:10.3402/nano.v4i0.22578.
7. P. Viste, J. Plain, R. Jaffiol, A. Vial, P.M. Adam, and and P. Royer. ACS Nano, **4**, 759 (2010). doi:10.1021/nn901294d. PMID:20050695.
8. D.J. Bergman and M.I. Stockman. Phys. Rev. Lett. **90**, 027402 (2003). doi:10.1103/PhysRevLett.90.027402. PMID:12570577.
9. Y. Yin, T. Qiu, J. Li, and and P.K. Chu. Nano Energy, **1**, 25 (2012). doi:10.1016/j.nanoen.2011.09.002.
10. Y. He, L.-M. Sai, H.-T. Lu, M. Hu, W.-Y. Lai, Q.-L. Fan, L.-H. Wang, and and W. Huang. Chem. Mater. **19**, 359 (2007). doi:10.1021/cm061863f.
11. P.C. Lee and D. Meisel. J. Phys. Chem. **86**, 3391 (1982). doi:10.1021/j100214a025.
12. W. Stöber, A., and E. Fink, and Bohn. J. Colloid Interface Sci. **26**, 62 (1968). doi:10.1016/0021-9797(68)90272-5.
13. S.C. Padmanabhan, J. McGrath, M. Bardosova, and M.E. Pemble, and J. Mater. Chem. **22**, 11978 (2012). doi:10.1039/C2JM31706K.
14. A.M. Saad, M.B. Mohamed, M.T.H. Abou, and I.M. Azzouz Kana. Opt. Laser Technol. **46**, 1 (2013). doi:10.1016/j.optlastec.2012.04.004.
15. H.E. Swanson and E. Tatge. Standard X-ray diffraction powder patterns, vol. I. National Bureau of standards, Washington, DC. 1953.
16. J.D. Jorgensen. J. Appl. Phys. **49**, 5473 (1978). doi:10.1063/1.324517.
17. H.E. Swanson and E. Tatge. *In* Monograph 25, Section 3. U.S. Dept. of Commerce, National Bureau of Standards: For sale by the Supt. of Docs., U.S. G.P.O., Washington, DC. 1953.
18. D. Magde, R. Wong, and and P.G. Seybold. J. Photochem. Photobiol. **75**, 327 (2002). doi:10.1562/0031-8655(2002)075<0327:FQYATR>2.0.CO;2.
19. K. Ray, R. Badugu, and and J.R. Lakowicz. J. Am. Chem. Soc. **128**, 8998 (2006). doi:10.1021/ja061762i. PMID:16834349.
20. J. Wang, J. Moore, S. Laulhe, M. Nantz, S. Achilefu, and and K.A. Kang. Nanotechnol. **23**, 095501 (2012). doi:10.1088/0957-4484/23/9/095501.
21. E. Rabani and R. Baer. Nano Lett. **8**, 4488 (2008). doi:10.1021/nl802443c. PMID:19367885.
22. Y. Kobayashi and N. Tamai. J. Phys. Chem. C, **114**, 17550 (2010). doi:10.1021/jp1063098.
23. M.C. Troparevsky and A. Franceschetti. App. Phys. Lett. **87**, 263115 (2005). doi:10.1063/1.2150583.
24. V.I. Klimov, A.A. Mikhailovsky, S. Xu, A. Malko, J.A. Hollingsworth, C.A. Leatherdale, H.-J. Eisler, and M.G. Bawendi. Sci. **290**, 314 (2000). doi:10.1126/science.290.5490.314.